White Rose Research Online

eprints@whiterose.ac.uk
https://eprints.whiterose.ac.uk
Universities of Leeds, Sheffield and York

Deposited via The University of York.

White Rose Research Online URL for this paper:
https://eprints.whiterose.ac.uk/id/eprint/238500/

Version: Accepted Version

Article:
HILL, JON (2026) The impact of antecedent topography on tsunami deposition. Natural Hazards. 254. ISSN: 1573-0840

https://doi.org/10.1007/s11069-026-08017-9

Reuse
This article is distributed under the terms of the Creative Commons Attribution (CC BY) licence. This licence allows you to distribute, remix, tweak, and build upon the work, even commercially, as long as you credit the authors for the original work. More information and the full terms of the licence here:
https://creativecommons.org/licenses/

Takedown
If you consider content in White Rose Research Online to be in breach of UK law, please notify us by emailing eprints@whiterose.ac.uk including the URL of the record and the reason for the withdrawal request.

UNIVERSITY OF LEEDS
University of Sheffield
UNIVERSITY of York

The impact of antecedent topography on tsunami deposition

Jon Hill[1*], Frances Taylor[1], Jeff Peakall[2], Gareth Keevil[2], Robert E. Thomas[2,3], Natasha L.M. Barlow[2], Elisabeth T. Bowman[4], David M. Hodgson[2], Georges Kesserwani[4]

[1]Department of Environment and Geography, University of York, UK.
[2]School of Earth and Environment, University of Leeds, UK.
[3]Energy and Environmental Institute, University of Hull, UK.
[4]School of Mechanical, Aerospace and Civil Engineering, University of Sheffield, UK.

*Corresponding author(s). E-mail(s): jon.hill@york.ac.uk;

Abstract

Tsunamis are potentially destructive events that occur due to disturbance of the sea floor, such as earthquakes or submarine landslides. Large tsunamis, such as the Japanese 2011 event, occur infrequently, so to establish long term tsunami records the sedimentary record can be used to extend the data and historic record to obtain a long term view. However, little is known about the depositional mechanisms that occur during tsunami waves. Whilst a number of tsunami deposits have been identified around the world, it is not understood how the deposit can be used to understand the wave dynamics. Here, we present a series of flume experiments to examine the depositional mechanisms of bore-type waves with differing antecedent topography. We used photogrammetry to examine the changes to the sedimentary bed pre- and post-wave train, with video used to examine sediment transport as the waves pass. A number of small cores were also examined as a proxy for what might be recovered during field-based studies. Sediment transport is primarily by near-bed or bedload transport, with lofting of sediment into the water column for larger waves. The experiments show deposition in depressions as well as in the onshore areas. The cores show no sedimentary structures that can be related to the wave forms, except for some winnowing of smaller grain sizes in erosive areas. Our results show the potential of performing flume experiments to understand tsunami dynamics which in turn will enable a greater understanding of palaeotsunami deposits.

Keywords: Tsunami, Wave, Flume, Tsunami Deposition

1 Introduction

Tsunamis are rare extreme events (Scheffers and Kelletat, 2003) that can leave behind a sedimentological signature (Costa and Andrade, 2020). Following 2004 (Indian Ocean) and 2011 (Japan), researchers rapidly collected sedimentological data from both these large tsunamis to decipher flow depths and velocities (Fritz et al., 2006; Foytong et al., 2013), inundation extent (Chagué-Goff et al., 2012), tsunami deposit thickness (Abe et al., 2012), grain-size distributions (Szczuciński et al., 2012), sedimentary structures (Naruse et al., 2012), and geochemical (Irizuki et al., 2019) and biological signals (Irizuki et al., 2019). However, even when combined with video footage, measured data, and interviews, it is still challenging to establish the exact flow conditions at a particular site with errors of up to 1 m/s (Foytong et al., 2013). This flow information is needed to both validate numerical models of hydrodynamics of past tsunamis and to study the long term tsunami record from sedimentary deposits, which will in turn enable risk analysis of coastlines prone to tsunami events (Tappin, 2007).

Given the challenges of obtaining hydrodynamic information from sediments alone, even where recorded data exist, it is more challenging to do so where these additional data do not exist. However, as large tsunamis are rare events, a long record is required to accurately assess the long-term risk posed (Kempf et al., 2017). We therefore must rely on palaeotsunamis, known only by their sedimentary deposit, to create these long records of events (Tappin, 2007). Palaeotsunamis, such as the Storegga Slide tsunami, left sedimentary deposits across a wide area (e.g. Hill et al., 2023; Smith et al., 2004; Tooley and Smith, 2005; Dawson and Smith, 2000; Dawson et al., 1988; Long et al., 2016; Svendsen and Mangerud, 1990; Bondevik et al., 2003; Vasskog et al., 2013; Grauert et al., 2001; Wagner et al., 2007). Recent analysis from these has shown it is possible to ascertain the number of waves in the tsunami wave train and the type of depositional mechanisms (Hill et al., 2023). Ideally, it would be possible to take a set of sedimentary deposits from a tsunami and invert those into hydrodynamic information, which can be used in conjunction with numerical models to recreate past tsunamis. To do this the relationship between flow behaviour and deposit needs to be understood.

Both physics-based and statistics-based models of the relationship between flow and deposits have been developed. Physics-based tsunami inversion models attempt to link the basic information of the tsunami deposits with the wave flow characteristics. There are four prominent physics-based inversion models: Moore's advection model (Moore et al., 2007); Soulsby's model (Soulsby et al., 2007), TsuSedMod model (Jaffe and Gelfenbuam, 2007), and TSUFLIND (Tang and Weiss, 2015) which is a combination of the three models with extensions. It should be noted that all models are based on a variety of basic assumptions and use different information obtained from the deposits. Models typically make assumptions on bedload or suspended sediment transport processes to use grain size data from a deposit to back-calculate velocity

and flow depth. More recently, statistical models using machine-learning techniques, such as Deep Neural Networks (DNN), have been used to invert sedimentary characteristics to flow characteristics without any explicit physical assumptions made (Mitra et al., 2020). These methods require a large database of deposits with known flow conditions, derived from numerical models, which are then used to train the machine learning algorithms. A deposit (or series of deposits) can then be used as inputs such that the DNN can estimate the flow characteristics. There are therefore implicit physical assumptions contained within the numerical model used to create the database of flow and deposits to train the model. Moreover, machine-learning techniques cannot be used to test ideas of depositional processes nor understand which processes are dominant in a particular deposit. Regardless of the type of inversion technique, both, either implicitly or explicitly, require a physical understanding of the sedimentary processes that dominate tsunami sediment deposition.

One solution to gaining a deeper understanding of tsunami deposition of sediments is to use flume-based studies (Yamaguchi and Sekiguchi, 2018, 2015; Shinozaki et al., 2020; Johnson et al., 2016; Yoshii et al., 2017). The aim of such flume-based studies is to understand the hydrodynamics and deposition processes involved in tsunamis in a controlled environment. All previous studies have done this by simulating the deposition process only; the wave passes over a sandy bed or dune where erosion takes place and the flow entrains sediment. The sediment that is now in suspension or transported as bedload is then carried to the deposition area. This has enabled the amount of sediment deposited to be calculated as a function of available sediment. However, erosion and deposition are not strictly delimited in space or time as a wave bore passes over a sediment bed (e.g. van der Zanden et al., 2019). Experiments of tsunami sedimentation thus far have noted the impact of hydraulic jumps in deposition (Yamaguchi and Sekiguchi, 2018; Yoshii et al., 2017; Yamaguchi and Sekiguchi, 2015) including immediately after the sand dune from where sediment is sourced (Yoshii et al., 2017). A hydraulic jump occurs when the flow moves from supercritical ($F_r > 1$) to subcritical ($F_r < 1$) and during that switch, deposition occurs. It is important to understand the mechanisms of both erosion and deposition as the tsunami deposit is a function of the source grain size distribution(s), the sorting processes that occur during transport and the local topography and environment (Shinozaki et al., 2020). Sorting can occur by both suspension of sediment followed by settling, but also in bedload transport (Steidtmann, 1982). Sediment in the bedload can be transferred to suspended load via turbulent processes, but this process depends on the shear and turbulent mixing (Chiodi et al., 2014). Recent work on tsunami sediments have speculated "vertical-pumping" may also keep any finer grains in suspension longer than would otherwise be suspected, meaning finer grains could be transported seaward via the backwash wave (Hill et al., 2023). Therefore, the characteristics of the local environment including vegetation and morphology, which play a role in the hydraulics of the wave, combined with the dominant processes occurring within the wave, will all impact the erosion and deposition of sediment.

Assumptions made in all inverse models and previous flume experiments are that: the deposit being analysed is formed by a single wave, deposition and erosion are separated, and the initial depositional topography is smooth. However, it is possible to

discern multiple waves from a sedimentary deposit, even if there are no clear structures to indicate this (Hill et al., 2023) and in reality erosion and deposition take place alongside each other on a non-uniform bed (van der Zanden et al., 2019). Here, we describe a number of experiments where three waves were passed over a sand layer to examine sedimentary processes during deposition. We describe the flume setup before detailing the findings from the experiments. We then show how the results of this study can be used to understand palaeotsunami deposits from cores or section in terms of wave dynamics during deposition.

2 Methods

2.1 Flume set-up

The flume was 5.0 m long, 0.50 m wide and 1.50 m deep. The floor sloped at 1.5° for all experiments (Fig. 1). The flume had a head tank installed with a liftable gate at 0 m and a 'beach' slope from 4 m to 5 m. The bed of the flume was covered 'roughness boards': glass beads of 1500-3000 μm diameter and fixed into place with Araldite. This procedure was carried out to prevent the sand from rolling back down under gravity on the 'beach' profile after the wave had been released and was determined experimentally. The mobile sediment was then added in a roughly 50 mm thick layer, wedge shaped, tapering to zero at both the start of the 'beach' slope (4 m) and the gate (0 m), and horizontal between 1 and 4 m distance along the flume. Two Nikon D7200 cameras were placed to view the wave. The first was a side view placed such that the final metre before the 'beach' slope was visible in the frame, and an overhead camera placed to view the 'beach' slope itself. Transparent rulers were fixed to the flume side to enable distance measurements on the video recordings. The video recordings were made at 1,920 x 1080 pixel resolution and 23.98 frames per second, using a light pulse to synchronise video frames from the two cameras. Ponded water of 50 mm height at 2 m distance was created, such that the water level was zero at the 'beach' slope. Three 4 MHz Ultrasonic Doppler Velocity Profiler (UDVP) probes were placed at 2 m from the head tank, mounted from above, which measured downstream along-flume velocity at 0, 20 and 40 mm heights (Fig. 1) to provide a near-bed velocity profile for shear calculations. The UDVPs measured speed at downstream distances of 5.245 to 74.159 mm from the probes. Results shown are from a downstream distance of 10.130 mm from the probe. The sand bed material consists of medium-grained sand with a D_{mean} of 216 μm and a D_{16} of 154 μm and D_{84} of 270 μm (Fig. 2).

Prior to the main experiments a number of small experiments were carried out to assess the effectiveness of the post-experiment analysis and to test the experimental set-up (see below). Two main experiments were carried out (Table 1). In the first set, the mobile sand layer was screed flat to create a smooth horizontal surface. The second experiment was similar, but was manually roughened following screeding. For each we ran three waves over the bed to simulate the total wave train passing over a site. For each experiment photogrammetry was used to capture the surface of the sand layer before and after the experiments. Due to the need to allow the sand to dry before commencing photogrammetry it was not possible to collect data between each wave.

2.2 Data collection

Around 75 to 150 images were manually captured, at 6,000 x 4,000 pixel resolution using a third Nikon D7200 camera, along the flume length using unique markers placed at 1 m intervals along the flume to aid the next step of processing. Image capture was carried out around 6 to 12 hours post experiment to allow the sand to fully dry as otherwise reflections from water and wet sand interfered with the photogrammetric processing. The photographs were then processed in Agisoft Metashape Professional (version 1.6.2 2020) to create a point cloud of the flume. However, these point clouds had no geostatic references so were in an arbitrary reference frame. CloudCompare (www.cloudcompare.org, version 2.9.1, 2019) was used to georeference point clouds using the known coordinates of four locations in the point clouds. Given the sediment was screed to a level surface (relative to the slope of the flume) these four locations were taken as zero height. A 3D Helmert transformation was then carried out to move, scale and rotate the point cloud coordinates to the real-world coordinates. This was repeated three times, but the transformation between iteration two and three was minimal. The transformation was such that the sediment bed was levelled (note that in reality the sediment bed would have been at an angle of 1.5 degrees to horizontal).

Once aligned, the point clouds were converted to raster format using GMT (Wessel et al., 2019) and then further analysed in QGIS (QGIS.org, 2020). Height data were extracted along the centre of the raster at 1 cm intervals and differences between post- and pre-experiment could be computing via the DEM of Difference. To examine the precision and accuracy of this technique a test experiment was used. Photograph sets were collected and processed independently of the same post-experiment bed. If the processing and alignment were perfectly accurate the difference between the two DEMs would be zero. The test showed a mean height difference of 0.026 mm, with a standard deviation of 1.013 mm (Fig. 3). Assuming that errors are independent and normally distributed (e.g. Lane et al., 1993; Passalacqua et al., 2015), we have selected a confidence interval of 85% (2 sigma). We have therefore used ± 2.026 mm (2σ) as our confidence interval in all results using the photogrammetry.

Cores were collected by placing a thin perspex square under the sand prior to set-up. Following the experiment, 25 mm diameter tubing was placed through the sand to the perspex sheet. The surrounding sand was removed and then tubing was removed, with the perspex in place. Resin was then placed in the tubing and left to set. The tubing was then cut open and the core removed. Cores were sliced vertically to create two halves; one of which was polished. The cores were photographed using a Zeiss Axio Zoom.v16 with Axiocam 105 colour camera to analyse grain size changes with depth. The core section was moved upwards a small amount after each photograph until the whole vertical core section was photographed. The photographs were then stitched together to produce a single image: a vertical section up the core. Two such transects were carried out per core (R1 and R2) along different vertical lines. Grain size distributions were estimated using an image processing algorithm following Ho et al. (2019), carried out in Matlab-2020-b.

Froude number was calculated by measuring the depth of the flow at each frame in the side-on video via pixel counting and scaling via the transparent rulers. The speed was taken from the UDVP probe at 20 mm height. Note the two measurements

are two metres apart, but the flow height stayed visually consistent between to two points. Further analysis of the video frames was carried out by stacking the a single pixel column through time. A total of 95 frames were stacked from capturing the passage of the wave at this fixed point. Similarly, Reynold's number were calculated using the depth of the flow and speed. Finally, shear velocity was calculated using the gradient of speed from the three UDVP probes to estimate $u_*\kappa$, which was then used to calculate Rouse number ($P = v_s/u_*\kappa$), and shear stress $\left(\tau = \rho u_*^2\right)$, where ρ is the density of water (1000 kg/m^3), κ is von Karman's constant (0.41) , and v_s is the settling velocity which was calculate using Stoke's formula and the D_50 grain size ($v_s = 0.03085236\, m/s$).

3 Results

3.1 Wave behaviour and visual sediment transport

The videos (see supplementary information) show that for all experiments the wave is a smooth bore-like wave, with no overturning at the head of the wave (Fig. 4). There is a clear relationship between the size of the wave and the amount the height the head tank was filled. The wave shape does vary between the two experiments. Experiment 1 (flat bed) produces a wave that slopes gently to a peak height before becoming almost flat on the top surface, with no clear indication of ripples or structure in the wave. Experiment 2 was similar but the wave shows undulations on the top surface up to centimetre-scale in amplitude. The wavelength of these varies with the wave height. As the wave approaches the 'beach' slope the wave shows evidence of a breaking front as it moves up-slope. This only occurs for the waves where the head tank fill level was 0.25 m or greater. Sediment deposition occurs from the base of the 'beach' slope to a distance less than the maximum inundation up-slope (Fig. 5). In experiment 1 the maximum inundation distance of the wave was beyond the edge of the slope, but the maximum distance of sediment deposition was around 60 cm up-slope. In experiment 2, sediment deposition occurred along the full distance of the slope. However, the wave readily surged past this point.

Sediment within the wave is moved as bedload and suspended load, although there was only a small amount of sediment in suspension (Fig. 6). For smaller waves there is very little sediment in suspension. The side view of waves shows a dense bedload being transported in the lower centimetre or less of the wave. The sediment in suspension appears rather uniform with no clear changes in colour to indicate changes in concentration. For experiment 2 the bedload behaves quite differently. There were clear waves of bedload sediment, which correspond to the undulation on the surface of the water, with greater wave depth generating more near-bed transport. Close inspection of the video indicates a slight diffusion of sediment from this near-bed layer to the suspended layer. In experiment 2.3 there is a clear water layer at the uppermost part of the wave, with suspended sediment concentration showing variability along the wave. This is not seen in experiment 1.2 or 1.3. The reflected wave has no sediment in the near-bed region and very little in suspension in all experiments.

3.2 Flow characteristics

Velocity probe data shows the speed difference in each wave height. For experiment 1, peak speed of the water is just over 1 m/s on the forward wave (Fig. 7). This is seen at all probe heights and occurs as the head of the wave reaches the probe location. The 0 mm probe shows the ponded water starting to move prior to the wave arrival, whereas probe locations 20 and 40 mm show no velocity until they are inundated, hence the sharp increase in water speed. After around 8 seconds the backwash wave is visible. The back wash wave is substantially slower, with a peak speed of less than 0.5 m/s in run 1. A similar pattern is seen in run 2, but with a lower maximum speed in the forward wave, 0.75 m/s, but the back wash wave is not substantially slower than in run 1. For the final run, the measured velocity peaks at 0.5 m/s for the forward wave and then quickly drops to near zero over 1-3 seconds. The backwash wave is also much slower.

The data for experiment 2 shows similar patterns (Fig. 7). Peak speed in run 1 is just over 1.25 m/s due to the higher head height. The reflected wave, again, takes around 8 seconds to arrive back at the probe, with peak speeds of around 0.5 m/s. Similar patterns are seen in runs 2 and 3; a peak speed that decreases with head height and a reflected wave returning at around 8 seconds and with peak speeds of 0.5 m/s.

The dimensionless parameters calculated (Rouse, Froude and Reynold's numbers) show some differences between experiments 1 and 2. The Froude number (Fig 8) shows repeated increases between sub- and super-critical for around 1 second in experiment 2 as the wave passes. All waves show a near critical Froude number for prolonged time, especially wave 1. In contrast, experiment 1 shows a steady decrease in Froude number from super-critical to sub-critical for all waves. Calculated Reynold's numbers are all above 5000 indicating turbulent flow. However, experiment 1.3 only reached significantly higher Reynolds numbers at the leading edge of the wave. Rouse number is generally above 2.5 indicating bedload transport. Experiment 2 shows an increasing Rouse number through time, increasing from values of around 1 to greater than 4, before stabilising around 4. This indicates a transition from suspended load to bedload transport as the wave progresses. Experiment 2.3 is quite variable, however. In contrast, experiment one rapidly increases above 2.5 and then is relatively stable. Note that values of zero indicate that the velocity gradient could not be calculated.

3.3 Bedforms and erosion/deposition

The DEMs show clear differences in the before and after experiment sediment surfaces (Fig. 9). For experiment 1 the differences are minor, with the velocity probe location clearly visible at 2 m. There is minor movement of bedforms (small undulations left by the screeding process) that show movement shoreward following the wave. These are highlighted in the transverse view (Fig. 10) as sinusoidal-like waves in the difference plot at 1 - 1.4 m and 3.2 - 4 m distance in the flume. However, these differences are smaller than the ± 2.026 mm confidence interval. The only statistically significant differences in the sediment bed for this experiment are at the velocity probe location and the first 0.1 m from the head tank where significant erosion occurred. Experiment 2 shows more substantial differences. In plan view (Fig. 9) there is 15 mm of deposition

extending up to 0.2 m of the head tank, followed by 15 mm of erosion extending to 1.0 m downstream of the head tank. There is then sustained deposition to around 2.5 m distance. Between 2.5 m and 3.7 m the surface is largely eroded, except for a small patch between 3 and 3.2 m in the centre of the flume. In the pre-experiment topography this is the location of a depression in the surface (Fig. 9). This has therefore been infilled by the waves passing over. The slope for the last metre of the flume shows minor deposition. These changes are reflected in the transverse view (Fig. 10). The erosion downstream of the head tank peaks at just over 15 mm, with up to 10 mm of deposition at the crest of the minor slope between 0.3 and 1 m distance. There is then sustained deposition, above the ± 2.026 mm confidence interval, to around 2.2 m distance. Much of the erosion between 2.2 and 4 m distance is not above the 2σ confidence interval (± 2.026 mm), but some peaks are significant (e.g. between 3.25 and 3.6 m) and are up to 5 mm of erosion. The infill of the depression is also clearly visible on the transverse view at 3 m distance with an increase of nearly 10 mm of height.

The three core sites showed little change in grain size (Fig. 11). Both replicates on each core show similar grain sizes and behaviour, but there are some differences in core 1.3, for example. For experiment 1 cores showed little variation in mean grain size throughout. Core 1.1 showed a slight coarsening at the top 1-2 mm, but only on the second replicate, and D_{16} does not increase. Core 1.3 showed a more substantial coarsening, from 200 to 300 μm in both replicates, but it is a similar grain size at the base of the core. However, the base of the core shows clear air bubbles preserved, which will be interpreted as larger grains by the analysis. For experiment 2 cores 1 and 2 showed a coarsening of grains in the top few millimetres from around 200 to over 300 μm. This is not seen in core 3, though there is substantial variation in grain size throughout that core. Note that the cores were located in erosive areas (Fig. 9) in experiment 2, though the erosion at the site of core 2 is very small. In experiment 1 there was very little erosion or deposition in the vicinity of the cores, but core 3 was located in an area of slight deposition, whilst core 2 was in an area of slight erosion. Core 1 in experiment 1 showed no height change.

Bedload transport for grains at the mean of the distribution would initiate at 0.17 N/m^2 bed shear stress (Shield's criterion). This is equivalent to around 0.24 m/s flow, not accounting for surface roughness or boundary effects of flow (e.g. Hutchins et al., 2023), which was exceeded at the probe location as the wave passed for all experiments. Moreover, the Rouse number shows a number of times above 2.5, indicating bedload transport. However, this fluctuates through time. Note that values of zero indicate there was no clear velocity gradient measured by the UDVP.

4 Discussion

Examining tsunami depositional mechanisms in a flume shows the importance of physical experiments for examining the basic underlying assumptions of both previous flume studies and inversion models. Sediment transport is shown to occur primarily as near-bed, with video images showing a dense layer of sediment at the base of the wave bore, with some sediment in suspension. The Rouse number indicate bedload transport at times, but with fluctuations. There is a marked difference between the initial

runs over flat beds, and subsequent runs that traverse topography created by the earlier flow(s). For instance, in experiment 1.1 over a flat bed, the sediment concentration in suspension increases from the head to the body of the bore, but there is only a very thin layer of dense sediment in the base of the flow. In contrast, in experiment 2.2 (same wave height as 1.1), there are very clear along-flow differences in the dense sediment layer at the base of the bore, with high intensity sediment bedload transport linked to smaller-scale waves superimposed on the main bore. Each of these smaller superimposed waves also leads to some of the material being incorporated into the suspended load. These structures are likely caused by undulations in the antecedent bed and seem to be visible as a "rolling" motion in the dense near-bed layer seen in experiment 2. Similarly, the Froude number shows a number of hydraulic jumps through time. The latter of these is particularly evident in experiment 2. Rouse numbers also show a contrast between experiment 1 and 2, with experiment 1 rapidly increasing to numbers above 2.5, whereas experiment 2 increases over time. These differences in sediment transport processes are thus entirely dependent on the nature of antecedent topography. It is also important to note that there is very little sediment in suspension in all experiments, despite the velocity of the water being sufficient to carry almost all grain sizes contained in the sediment bed as suspended load. This corresponds with the Rouse numbers calculated which indicate predominantly bedload transport. Analyses of tidal bores show similar transport mechanisms, with small Kelvin-Helmholtz-like structures along the base lofting sediment into suspension (Masunaga et al., 2015). These KH-like structures generate internal velocity variations in the form of vortices, as interpreted in Masunaga et al. (2015). The vortices can lift sediment into suspension near to the bed, but since they also contain downward velocity as the vortex rotates, the sediment will be kept in suspension near the bed.

These differences between runs over flat beds and undulating beds, may also be expected to lead to changes in sediment sorting. The more continuous sediment transport over flat beds, would be expected to lead to progressive size sorting of the bedload material (e.g. Ferdowsi et al., 2017). In contrast, over undulating topography, the short length-scales of the subsidiary waves lead only to periodic bedload or near-bed transport, with repeated entrainment and deposition, and thus the degree of longitudinal grain-size segregation is likely to be more limited. The periodic vortices associated with the smaller-scale waves, may also act as a 'vertical pump' to suspend sediment, as observed in studies of other wave trains (O'Hara Murray et al., 2012), perhaps locally removing fines.

The cores in experiment 1 show no grain size changes (Fig. 11). This matches the photogrammetric results since there are no discernible height changes. The cores for experiment 2 show some coarsening towards the top few millimetres which matches the amount of erosion in the area. For each core location in experiment 2, the core experienced either erosion or no significant change. The erosion is around 0.5 mm, which corresponds to a coarsening in both cores 1 and 2. Core 3 was located where there was no perceptible difference in topography and this core, though short, does not show any coarsening. The coarsening in the uppermost parts of the cores could be due to the bore either: i) picking up finer sediment, leaving coarser grains behind, ii) through eroding all the sediment, and then redepositing the coarser-grained fractions,

whilst transporting the fines in suspension., or iii) kinetic sieving, which has been observed in previous tsunami experiments (Yoshii et al., 2018). In all cases the bed would be winnowed and armoured, leading to a coarser layer at the top of the bed. However, given that coarsening at the top of cores is only observed in those areas that had undergone erosion, then this suggests that the second mechanism is the primary control. Where there was no elevation change, it appears that winnowing of finer-grained material whilst leaving coarser-grained material behind, was insufficient for a grain-size change to be observed. A wider sediment grain size distribution would further help to separate out the potential mechanisms.

Sediment deposition on the 'beach' slope is as expected, with deposition occurring to a distance that is less than the inundation distance. However, the elevation change is not statistically significant at the 2σ level (± 2.026 mm), indicating very little sediment was entrained and deposited. However, unlike previous experiments (e.g. Yamaguchi and Sekiguchi, 2018, 2015; Shinozaki et al., 2020; Johnson et al., 2016; Yoshii et al., 2017) that used a measured volume of sediment in a 'pick-up' zone to examine sediment deposition, a more realistic set-up was used here where erosion and deposition could occur along the full length of the flume. Moreover, running a sequence of waves is also more realistic compared to a real tsunami and the individual waves can be observed in field cores for palaeotsunami deposits (e.g. Hill et al., 2023). However, most change to the topography was visually observed in the largest waves, which then explains the lack of structures within the cores. The observations of high-concentration near-bed transport, fits with field data from the Storegga tsunami at Ythan, Scotland, that show a lack of grading at the base of deposits (e.g. Hill et al., 2023). These deposits are also poorly to very poorly sorted, reflecting rapid capacity-driven deposition as the flow decelerates. Such deposition may be expected to have happened on the 'beach' slope of the present experiments, however, the sediment grain size distribution was too narrow and the transported sediment volume too low to observe this.

Overall, our results show that the antecedent topography is a factor that needs considering when studying tsunami depositional mechanisms. The antecedent topography that the wave travels over alters both the sediment transport mechanisms and the depositional history. All previous work in flume studies have considered a 'pick-up' area for sediment and studied the deposition process alone. Likewise, tsunami sediment inversion algorithms contain assumptions on the depositional mechanisms which do not account for any antecedent topographic effects.

4.1 Limitations and future work

The lack of substantial grain size change seen in the cores can be explained by the narrow distribution of grain sizes in the bed sediment. Bedload transport for grains at the mean of the distribution would initiate at around 0.24 m/s flow, using Shield's criterion and Law of the Wall assumptions (Soulsby, 1997). Likewise the upper end of the distribution would be mobile at around 0.3 m/s. A wider distribution of grains would therefore allow better determination of possible mechanisms of transport under tsunami-like waves and explore effects such as surface roughness on erosion and transport under such mechanisms.

The drying process required to use the photogrammetry effectively reduced the number of times this method could be used. The reflections caused by wet sediment caused a number of stereo matching errors. Ideally, the photogrammetry would have been carried out between each wave for experiments 1 and 2 to determine how much change occurred between each wave. However, to do so would have meant waiting for the bed to completely dry, which then would have posed issues with refilling the flume with the ponded water again, disturbing the sediment surface and therefore invalidating the experiment. Other technologies such as water penetrating (green) LiDAR may work better and will be tried in future experiments.

5 Conclusion

Here we utilise physical experiments to demonstrate that antecedent topography plays a major role for both deposition and erosion of sediment under a tsunami-like bore wave. This topography triggers changes in the nature of the bore-wave, leading to a series of distinctive smaller waves superimposed on the main bore. Each of these smaller waves and its associated vortex is associated with enhanced sediment transport, dominantly bedload, alongside smaller increases in suspended sediment load. These results are in keeping with field data from the Storegga tsunami deposits from the Ythan Valley, Scotland, where it was conjectured that sediment transport appears to be largely contained in a dense layer at the base of the flow, not fully by suspension. The present experiments, however, show that in such settings there can be high-frequency pulsing of sediment concentration. Such localised and periodic transport of sediment, may not lead to rapid grain-size segregation, as would be anticipated in systems with more continuous and uniform sediment transport. Here we also show the ability of tsunami-like bore waves to lead to a coarsening of the grain-size of the uppermost parts of areas that were dominantly affected by flow bypass or minor erosion. We postulate that this coarsening is likely due to bed armouring through preferential winnowing of the fines. These impacts need to be considered in future flume experiment and in tsunami sediment inversion studies. These experiments should therefore be useful for future tsunami sediment experiments that include both deposition and erosion, and numerical model development.

6 Supplementary info

Videos for each experiment are included in the supplementary information. For review the videos are available in Google drive

7 Statements and Declarations

This work was support by the White Rose University Consortium Fund (INUNDATION project) awarded to JH, JP, GK, NLMB, ETB, and DMH.

The authors have no relevant financial or non-financial interests to disclose.

Acknowledgements

This project formed part of FT's BSc project supervised by JH, JP, GK and RT.

References

Abe, T., Goto, K., Sugawara, D.: Relationship between the maximum extent of tsunami sand and the inundation limit of the 2011 Tohoku-oki tsunami on the Sendai Plain, Japan. Sedimentary geology **282**(0), 142–150 (2012) https://doi.org/10.1016/j.sedgeo.2012.05.004

Bondevik, S., Mangerud, J., Dawson, S., Dawson, A., Lohne, Ø.: Record-breaking height for 8000-year-old tsunami in the North Atlantic. Eos, Transactions American Geophysical Union **84**(31), 289–293 (2003) https://doi.org/10.1029/2003EO310001

Costa, P.J.M., Andrade, C.: Tsunami deposits: Present knowledge and future challenges. Sedimentology **67**(3), 1189–1206 (2020) https://doi.org/10.1111/sed.12724

Chiodi, F., Claudin, P., Andreotti, B.: A two-phase flow model of sediment transport: transition from bedload to suspended load. Journal of fluid mechanics **755**, 561–581 (2014) https://doi.org/10.1017/jfm.2014.422

Chagué-Goff, C., Andrew, A., Szczuciński, W., Goff, J., Nishimura, Y.: Geochemical signatures up to the maximum inundation of the 2011 Tohoku-oki tsunami — Implications for the 869 AD Jogan and other palaeotsunamis. Sedimentary geology **282**, 65–77 (2012) https://doi.org/10.1016/j.sedgeo.2012.05.021

Dawson, A.G., Long, D., Smith, D.E.: The Storegga Slides: Evidence from eastern Scotland for a possible tsunami. Marine Geology **82**(3), 271–276 (1988) https://doi.org/10.1016/0025-3227(88)90146-6

Dawson, S., Smith, D.E.: The sedimentology of Middle Holocene tsunami facies in northern Sutherland, Scotland, UK. Marine Geology **170**(1), 69–79 (2000) https://doi.org/10.1016/S0025-3227(00)00066-9

Fritz, H.M., Borrero, J.C., Synolakis, C.E., Yoo, J.: 2004 Indian Ocean tsunami flow velocity measurements from survivor videos. Geophysical Research Letters **33**(24) (2006) https://doi.org/10.1029/2006GL026784

Ferdowsi, B., Ortiz, C.P., Houssais, M., Jerolmack, D.J.: River-bed armouring as a granular segregation phenomenon. Nature Communications **8**(1), 1363 (2017) https://doi.org/10.1038/s41467-017-01681-3

Foytong, P., Ruangrassamee, A., Shoji, G., Hiraki, Y., Ezura, Y.: Analysis of Tsunami Flow Velocities during the March 2011 Tohoku, Japan, Tsunami. Earthquake Spectra **29**(1_suppl), 161–181 (2013) https://doi.org/10.1193/1.4000128

Grauert, M., Björck, S., Bondevik, S.: Storegga tsunami deposits in a coastal lake on Suouroy, the Faroe Islands. Boreas **30**(4), 263–271 (2001) https://doi.org/10.1111/j.1502-3885.2001.tb01045.x

Ho, V.L., Dorrell, R.M., Keevil, G.M., Thomas, R.E., Burns, A.D., Baas, J.H., McCaffrey, W.D.: Dynamics and deposition of sediment-bearing multi-pulsed flows and geological implication. Journal of sedimentary research **89**(11), 1127–1139 (2019) https://doi.org/10.2110/jsr.2019.62

Hutchins, N., Ganapathisubramani, B., Schultz, M.P., Pullin, D.I.: Defining an equivalent homogeneous roughness length for turbulent boundary layers developing over patchy or heterogeneous surfaces. Ocean engineering **271**(113454), 113454 (2023) https://doi.org/10.1016/j.oceaneng.2022.113454

Hill, J., Rush, G., Peakall, J., Johnson, M., Hodson, L., Barlow, N.L.M., Bowman, E.T., Gehrels, W.R., Hodgson, D.M., Kesserwani, G.: Resolving tsunami wave dynamics: Integrating sedimentology and numerical modelling. The depositional record (2023) https://doi.org/10.1002/dep2.247

Irizuki, T., Fujiwara, O., Yoshioka, K., Suzuki, A., Tanaka, Y., Nagao, M., Kawagata, S., Kawano, S., Nishimura, O.: Geochemical and micropaleontological impacts caused by the 2011 Tohoku-oki tsunami in Matsushima Bay, northeastern Japan. Marine geology **407**, 261–274 (2019) https://doi.org/10.1016/j.margeo.2018.10.007

Johnson, J.P.L., Delbecq, K., Kim, W., Mohrig, D.: Experimental tsunami deposits: Linking hydrodynamics to sediment entrainment, advection lengths and downstream fining. Geomorphology **253**, 478–490 (2016) https://doi.org/10.1016/j.geomorph.2015.11.004

Jaffe, B.E., Gelfenbuam, G.: A simple model for calculating tsunami flow speed from tsunami deposits. Sedimentary geology **200**(3–4), 347–361 (2007) https://doi.org/10.1016/j.sedgeo.2007.01.013

Kempf, P., Moernaut, J., Van Daele, M., Vandoorne, W., Pino, M., Urrutia, R., De Batist, M.: Coastal lake sediments reveal 5500 years of tsunami history in south central Chile. Quaternary science reviews **161**, 99–116 (2017) https://doi.org/10.1016/j.quascirev.2017.02.018

Long, A.J., Barlow, N.L.M., Dawson, S., Hill, J., Innes, J.B., Kelham, C., Milne, F.D., Dawson, A.: Lateglacial and Holocene relative sea-level changes and first evidence for the Storegga tsunami in Sutherland, Scotland. Journal of Quaternary Science **31**(3), 239–255 (2016) https://doi.org/10.1002/jqs.2862

Lane, S.N., Richards, K.S., Chandler, J.H.: Developments in photogrammetry; the geomorphological potential. Progress in Physical Geography **17**(3), 306–328 (1993) https://doi.org/10.1177/030913339301700302

Masunaga, E., Homma, H., Yamazaki, H., Fringer, O.B., Nagai, T., Kitade, Y., Okayasu, A.: Mixing and sediment resuspension associated with internal bores in a shallow bay. Continental shelf research **110**, 85–99 (2015) https://doi.org/10.1016/j.csr.2015.09.022

Moore, A.L., McAdoo, B.G., Ruffman, A.: Landward fining from multiple sources in a sand sheet deposited by the 1929 Grand Banks tsunami, Newfoundland. Sedimentary geology **200**(3-4), 336–346 (2007) https://doi.org/10.1016/j.sedgeo.2007.01.012

Mitra, R., Naruse, H., Abe, T.: Estimation of tsunami characteristics from deposits: Inverse modeling using a deep-learning neural network. Journal of geophysical research. Earth surface **125**(9) (2020) https://doi.org/10.1029/2020jf005583

Naruse, H., Arai, K., Matsumoto, D., Takahashi, H., Yamashita, S., Tanaka, G., Murayama, M.: Sedimentary features observed in the tsunami deposits at Rikuzentakata City. Sedimentary geology **282**(0), 199–215 (2012) https://doi.org/10.1016/j.sedgeo.2012.08.012

O'Hara Murray, R.B., Hodgson, D.M., Thorne, P.D.: Wave groups and sediment resuspension processes over evolving sandy bedforms. Continental Shelf Research **46**, 16–30 (2012) https://doi.org/10.1016/j.csr.2012.02.011

Passalacqua, P., Belmont, P., Staley, D.M., Simley, J.D., Arrowsmith, J.R., Bode, C.A., Crosby, C., DeLong, S.B., Glenn, N.F., Kelly, S.A., Lague, D., Sangireddy, H., Schaffrath, K., Tarboton, D.G., Wasklewicz, T., Wheaton, J.M.: Analyzing high resolution topography for advancing the understanding of mass and energy transfer through landscapes: A review. Earth-Science Reviews **148**, 174–193 (2015) https://doi.org/10.1016/j.earscirev.2015.05.012

QGIS.org: QGIS Geographic Information System. Open Source Geospatial Foundation Project (2020)

Scheffers, A., Kelletat, D.: Sedimentologic and geomorphologic tsunami imprints worldwide—a review. Earth-Science Reviews **63**(1–2), 83–92 (2003) https://doi.org/10.1016/S0012-8252(03)00018-7

Szczuciński, W., Kokociński, M., Rzeszewski, M., Chagué-Goff, C., Cachão, M., Goto, K., Sugawara, D.: Sediment sources and sedimentation processes of 2011 Tohoku-oki tsunami deposits on the Sendai Plain, Japan — Insights from diatoms, nannoliths and grain size distribution. Sedimentary geology **282**(0), 40–56 (2012) https://doi.org/10.1016/j.sedgeo.2012.07.019

Svendsen, J., Mangerud, J.: Sea-level changes and pollen stratigraphy on the outer coast of Sunnmøre, western Norway. Norsk Geologisk Tidsskrift (1990)

Soulsby, R.: Dynamics of Marine Sands: a Manual for Practical Applications. Thomas

Telford, London (1997)

Smith, D.E., Shi, S., Cullingford, R.A., Dawson, A.G., Dawson, S., Firth, C.R., Foster, I.D.L., Fretwell, P.T., Haggart, B.A., Holloway, L.K., Long, D.: The Holocene Storegga Slide tsunami in the United Kingdom. Quaternary Science Reviews **23**(23), 2291–2321 (2004) https://doi.org/10.1016/j.quascirev.2004.04.001

Soulsby, R.L., Smith, D.E., Ruffman, A.: Reconstructing tsunami run-up from sedimentary characteristics: A simple mathematical model. In: Coastal Sediments 07. American Society of Civil Engineers, Reston, VA (2007). https://doi.org/10.1061/40926(239)83

Steidtmann, J.R.: Size–density sorting of sand-size spheres during deposition from bedload transport and implications concerning hydraulic equivalence. Sedimentology **29**(6), 877–883 (1982) https://doi.org/10.1111/j.1365-3091.1982.tb00090.x

Shinozaki, T., Yamaguchi, N., Sekiguchi, T.: Flume experiments test grain-size distribution of onshore tsunami deposits. Sedimentary geology, 105750 (2020) https://doi.org/10.1016/j.sedgeo.2020.105750

Tappin, D.R.: Sedimentary features of tsunami deposits—their origin, recognition and discrimination: an introduction. Sedimentary geology **200**(3), 151–154 (2007)

Tooley, M.J., Smith, D.E.: Relative sea-level change and evidence for the Holocene Storegga Slide tsunami from a high-energy coastal environment: Cocklemill Burn, Fife, Scotland, UK. Quaternary International **133**(0), 107–119 (2005) https://doi.org/10.1016/j.quaint.2004.10.007

Tang, H., Weiss, R.: A model for tsunami flow inversion from deposits (TSUFLIND). Marine geology **370**, 55–62 (2015) https://doi.org/10.1016/j.margeo.2015.10.011

Zanden, J., Cáceres, I., Eichentopf, S., Ribberink, J.S., Werf, J.J., Alsina, J.M.: Sand transport processes and bed level changes induced by two alternating laboratory swash events. Coastal engineering **152**(103519), 103519 (2019) https://doi.org/10.1016/j.coastaleng.2019.103519

Vasskog, K., Waldmann, N., Bondevik, S., Nesje, A., Chapron, E., Ariztegui, D.: Evidence for Storegga tsunami run-up at the head of Nordfjord, western Norway. Journal of Quaternary Science **28**(4), 391–402 (2013) https://doi.org/10.1002/jqs.2633

Wagner, B., Bennike, O., Klug, M., Cremer, H.: First indication of Storegga tsunami deposits from East Greenland. Journal of Quaternary Science **22**(4), 321–325 (2007) https://doi.org/10.1002/jqs.1064

Wessel, P., Luis, J.F., Uieda, L., Scharroo, R., Wobbe, F., Smith, W.H.F., Tian, D.: The generic mapping tools version 6. Geochemistry, geophysics, geosystems: G(3)

20(11), 5556–5564 (2019) https://doi.org/10.1029/2019gc008515

Yamaguchi, N., Sekiguchi, T.: Effects of tsunami magnitude and terrestrial topography on sedimentary processes and distribution of tsunami deposits in flume experiments. Sedimentary geology **328**, 115–121 (2015) https://doi.org/10.1016/j.sedgeo.2015.08.008

Yamaguchi, N., Sekiguchi, T.: Sedimentary Processes and the Distribution of Tsunami Deposits On a Narrow Coastal Lowland Backed By a Cliff in Flume Experiments. Journal of Sedimentary Research **88**(4), 467–474 (2018) https://doi.org/10.2110/jsr.2018.25

Yoshii, T., Tanaka, S., Matsuyama, M.: Tsunami deposits in a super-large wave flume. Marine geology **391**(Supplement C), 98–107 (2017) https://doi.org/10.1016/j.margeo.2017.07.020

Yoshii, T., Tanaka, S., Matsuyama, M.: Tsunami inundation, sediment transport, and deposition process of tsunami deposits on coastal lowland inferred from the Tsunami Sand Transport Laboratory Experiment (TSTLE). Marine geology **400**, 107–118 (2018) https://doi.org/10.1016/j.margeo.2018.03.007

Tables and Figures

Table 1 Experimental set-up for all experiments described here.

Experiment number	Head height (m)	Starting topography	Photogrammetry
Test	0.20	Flat	Post (twice)
1.1	0.25	Flat	Pre
1.2	0.20	From experiment 1.1	
1.3	0.15	From experiment 1.2	Post
2.1	0.30	Manually roughened	Pre
2.2	0.25	From experiment 2.1	
2.3	0.20	From experiment 2.2	Post

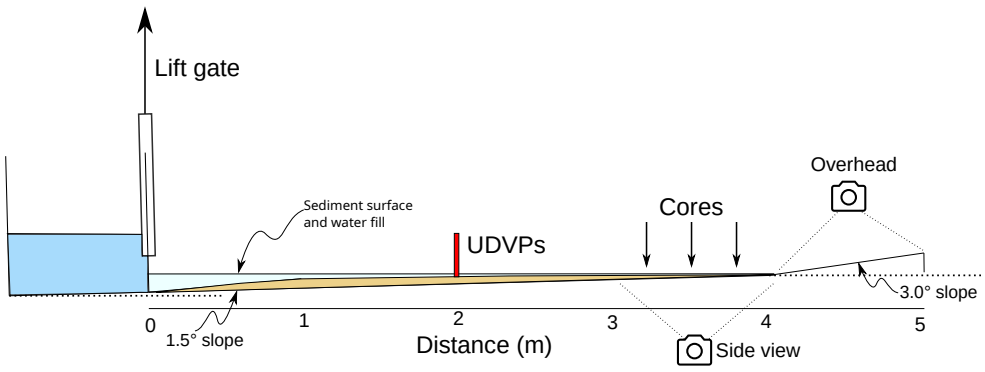

Fig. 1 Flume setup.

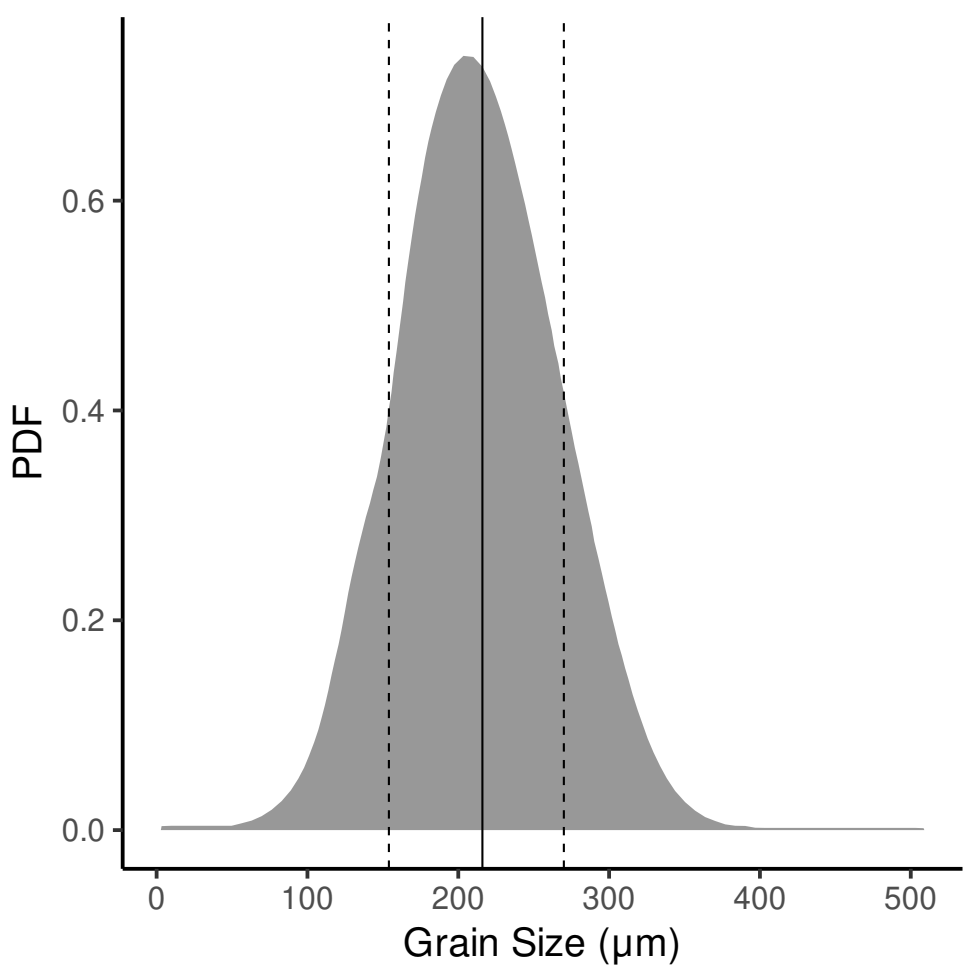

Fig. 2 Probability density function of the grain size of the sediment used in all experiments. Solid line indicates the mean grain size (216 μm) and the two dashed lines represent the D_{16} (154 μm) and D_{84} (270 μm) percentiles respectively.

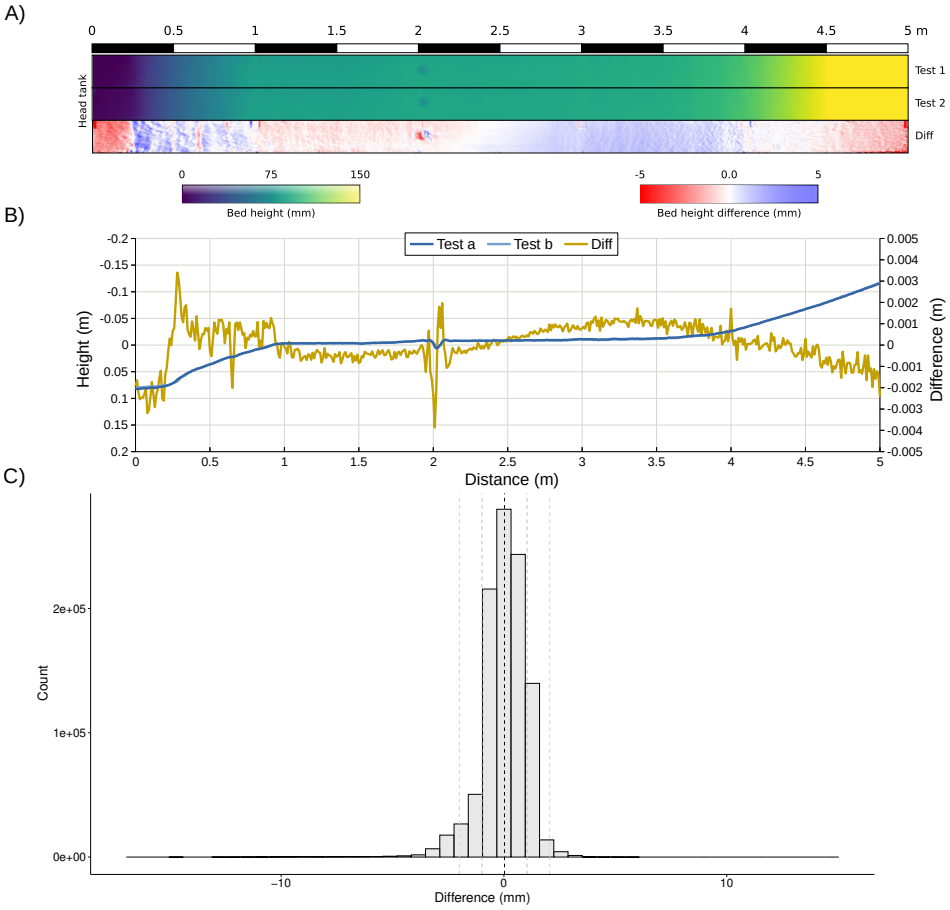

Fig. 3 Validation of the point cloud alignment and sensitivity to differences. A) Colour images of bed height for tests 1 and 2, with the difference shown beneath. B) Line plot along the centre of the rasterised point cloud data showing height on the left axis and difference on the right axis. C) Distribution of difference in the two independent sets of photogrammetry results. Mean difference is 0.026 mm, standard deviation (σ) is 1.013 mm. Vertical lines indicate the mean, 1σ and 2σ.

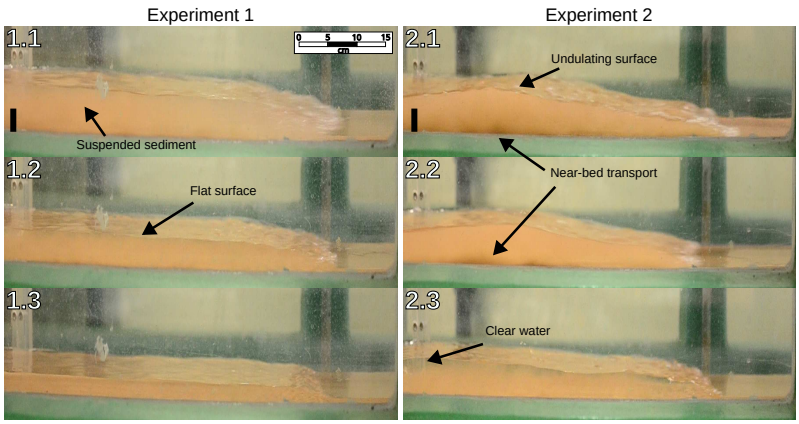

Fig. 4 Side view of the wave from each experiment. The horizontal scale is shown by the ruler. Vertical scale is shown by the black bar (4 cm) and the vertical has been exaggerated by a factor of 2.

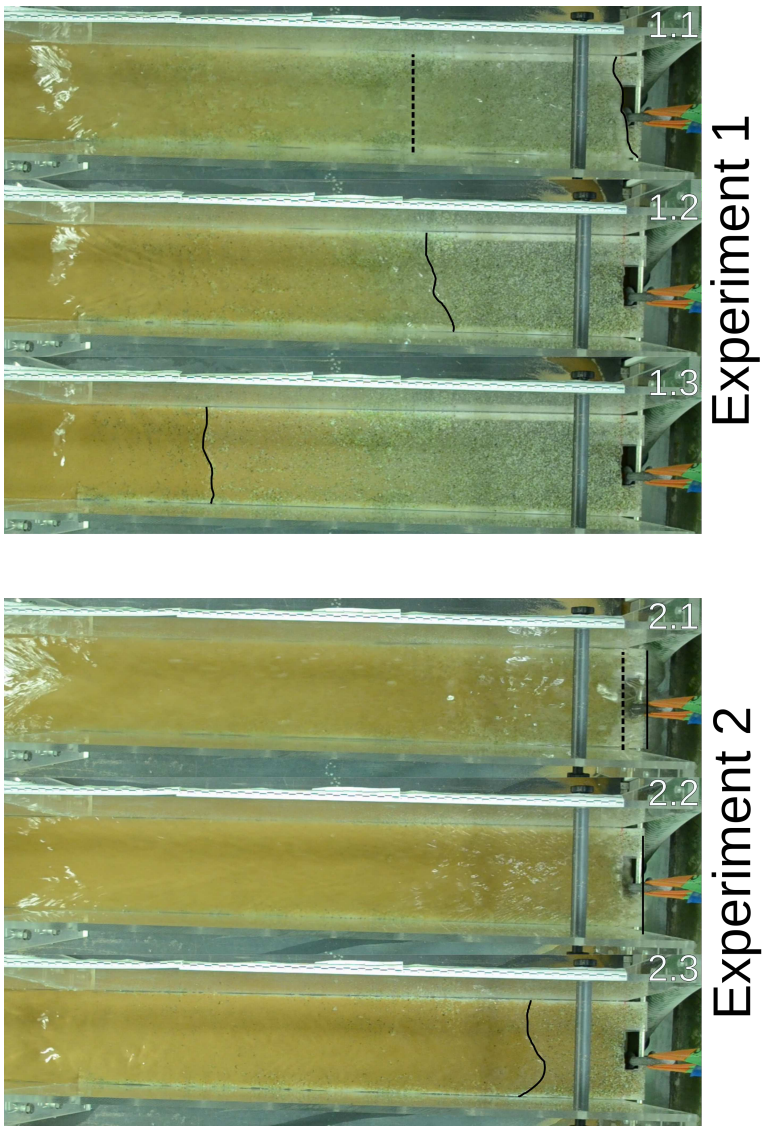

Fig. 5 Top-down view at time of maximum inundation. Dotted line shows the approximate maximum sediment deposition for the first run in the two experiments (subsequent runs did not deposit sediment as far as the first run). The solid black line denotes the approximate maximum inundation limit of the wave. Where the wave passes over the edge of the flume, the solid line is along that edge.

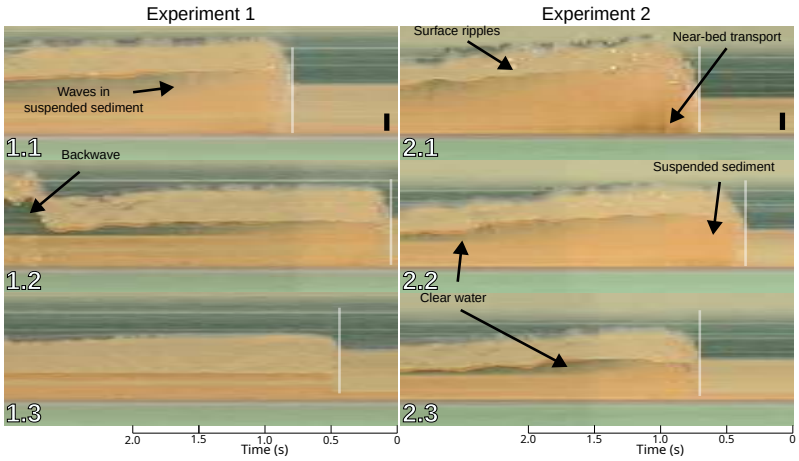

Fig. 6 Composite frame side view of the waveform from each experiment at a fixed point in space and arranged in time order. Horizontal axis is time (s), with the vertical exaggerated by a factor of 2; black bar represents 2 cm.

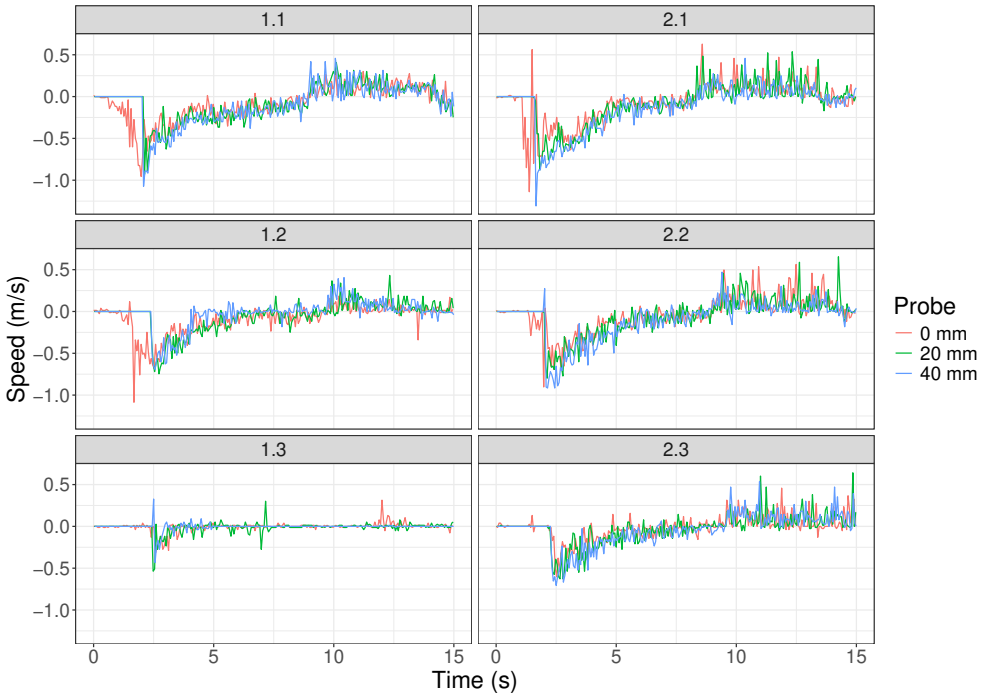

Fig. 7 Speed at the probe. Colour indicate the probe height above the bed (as indicated in the key) with each experiment labelled. Speed is measured downstream such that negative numbers indicate flow towards the beach end of the flume and positive numbers indicate flow towards the head tank. All data were recorded at a distance of 10.13 mm from the probe in the downstream direction.

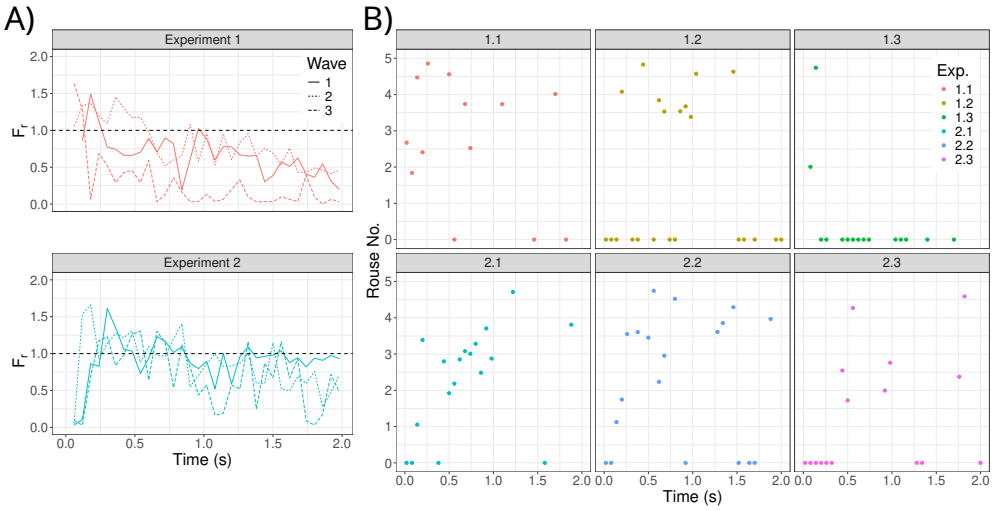

Fig. 8 Froude (A) and Rouse (B) numbers for each experiment. Experiments 1.1 to 1.3 and 2.1 to 2.3 are shown on the same plot for Froude number for comparison. Rouse number is plotted separately for each experiment (1.1 to 2.3) for for clarity.

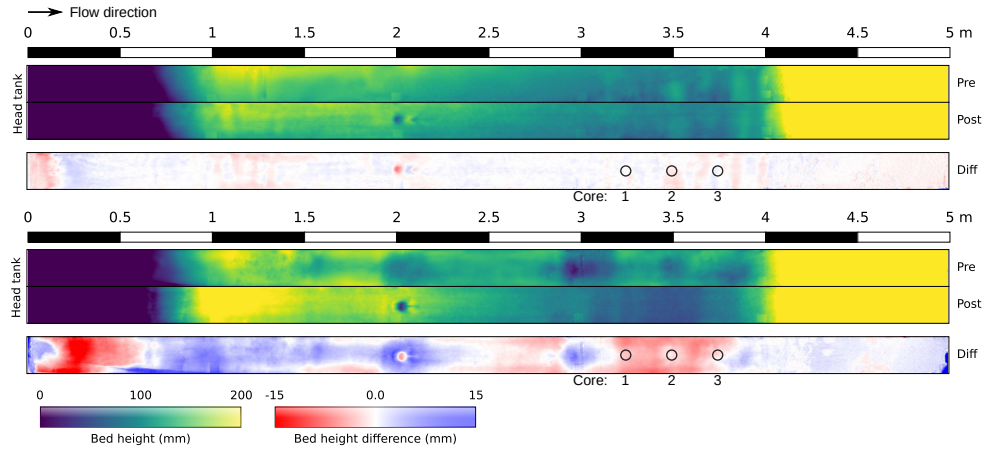

Fig. 9 Before and after DEMs of the bed surface for experiments 1 (top) and 2 (bottom). The difference between the pre- and post-experiment photogrammetry is shown below each pair. The black circles on the difference plot shows the location of the cores taken.

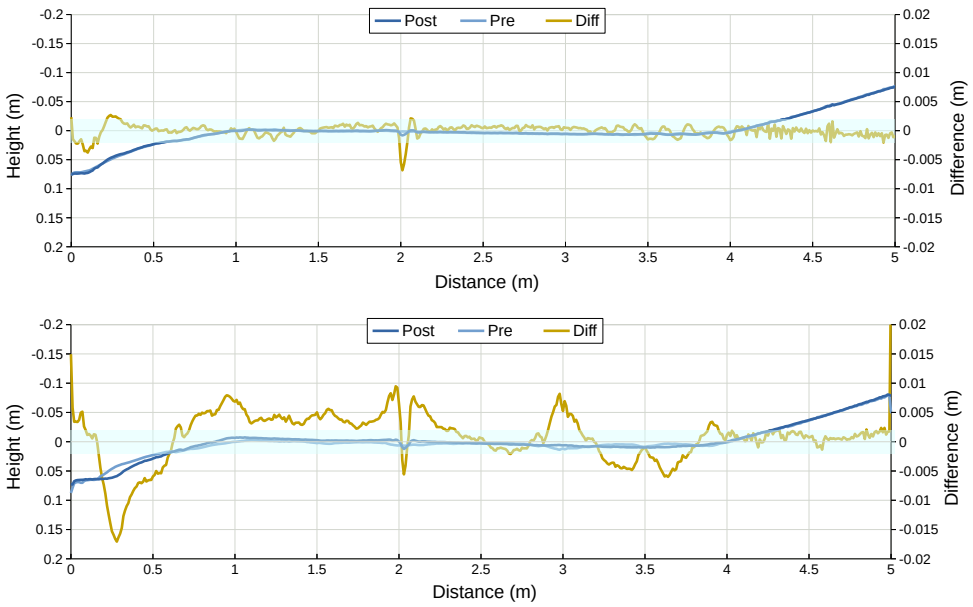

Fig. 10 Profiles from the centre of the flume extracted from the DEM. Difference is plotted in yellow. Blue box indicates confidence interval from the difference histogram (Fig. 3)

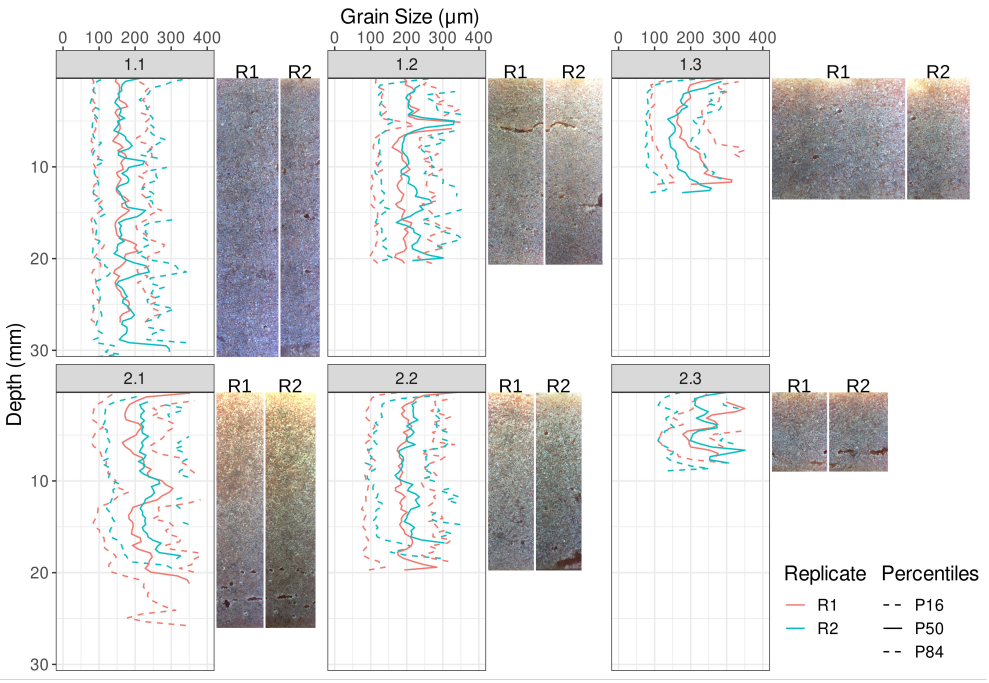

Fig. 11 Grain size analysis, d16, d50 and d84, for the cores calculated using image processing in Matlab. Two replicates (R1 and R2) are shown for each core. The image used for each analysis is shown to the right of each graph.